INSTITUTE OF PHYSICS PUBLISHING PHYSICS IN MEDICINE AND BIOLOGY

Phys. Med. Biol. **49** (2004) 4239–4258 PII: S0031-9155(04)82704-0

Statistical list-mode image reconstruction for the high resolution research tomograph

A Rahmim[1], M Lenox[2], A J Reader[3], C Michel[4], Z Burbar[4], T J Ruth[5] and V Sossi[1]

[1] Department of Physics and Astronomy, University of British Columbia, Vancouver, BC, Canada
[2] Concorde Microsystems, Knoxville, TN, USA
[3] Department of Instrumentation and Analytical Science UMIST, Manchester, UK
[4] CPS Innovations, Knoxville, TN, USA
[5] UBC/Triumf, Vancouver, BC, Canada

E-mail: rahmim@physics.ubc.ca, mlenox@cms-asic.com, andrew.j.reader@umist.ac.uk, Christian.Michel@cpspet.com, Ziad.Burbar@cpspet.com, truth@triumf.ca and vesna@physics.ubc.ca

Received 29 June 2004
Published 27 August 2004
Online at stacks.iop.org/PMB/49/4239
doi:10.1088/0031-9155/49/18/004

Abstract

We have investigated statistical list-mode reconstruction applicable to a depth-encoding high resolution research tomograph. An *image* non-negativity constraint has been employed in the reconstructions and is shown to effectively remove the overestimation bias introduced by the sinogram non-negativity constraint. We have furthermore implemented a convergent subsetized (CS) list-mode reconstruction algorithm, based on previous work (Hsiao *et al* 2002 *Conf. Rec. SPIE Med. Imaging* **4684** 10–19; Hsiao *et al* 2002 *Conf. Rec. IEEE Int. Symp. Biomed. Imaging* 409–12) on convergent histogram OSEM reconstruction. We have demonstrated that the first step of the convergent algorithm is exactly equivalent (unlike the histogram-mode case) to the regular subsetized list-mode EM algorithm, while the second and final step takes the form of additive updates in image space. We have shown that in terms of contrast, noise as well as FWHM width behaviour, the CS algorithm is robust and does not result in limit cycles. A hybrid algorithm based on the ordinary and the convergent algorithms is also proposed, and is shown to combine the advantages of the two algorithms (i.e. it is able to reach a higher image quality in fewer iterations while maintaining the convergent behaviour), making the hybrid approach a good alternative to the ordinary subsetized list-mode EM algorithm.

1. Introduction

In positron emission tomography (PET) systems, there is a continuous effort to increase sensitivity and to improve spatial resolution. This, in turn, brings about the need for different approaches to data collection and image reconstruction in order to make use of the high sampling capabilities of such systems. Conventional tomographs inherently bin the collected data into sinogram bins. In the case of high resolution tomographs with list-mode acquisition capability, such as the new high resolution research tomograph (HRRT) (Wienhard *et al* 2002), it is worthwhile to investigate the applicability of list-mode reconstruction schemes. For instance, in dynamic PET studies in which multiple low-statistics 3D PET scans are acquired, list-mode reconstruction can in principle be performed more quickly and efficiently than histogram-mode reconstruction: when the reconstruction of short time frames is required, the number of events acquired may in fact be less than the number of lines of response (LORs) in a full sinogram set.

Furthermore, when histogram-mode reconstruction methods are used, the data are often compressed in the axial or radial directions in order to accelerate the reconstruction tasks. This is sometimes referred to as *data mashing* by which it is meant that certain 'nearby' LORs are histogrammed into the same sinogram bin in order to reduce the size of the sinogram data. For instance, in the case of the HRRT, with no data compression, the sinogram size is 1.5 Gbytes. Application of axial/radial compression schemes, however, has been shown to adversely affect axial/transaxial resolution of images reconstructed using 3D-OSEM, especially as one moves away from the centre of the field-of-view (FOV) (Wienhard *et al* 2002). In the case of list-mode reconstruction, since events are considered one by one, sinogram data compression is in principle not needed, thus resulting in better image resolution and uniformity at no extra cost in terms of time and data size.

An additional advantage of list-mode reconstruction is the increased accuracy with which motion correction can be implemented into the reconstruction procedure (Rahmim *et al* 2003). This is the case since in histogram-mode reconstruction, a motion-corrected LOR will not typically correspond exactly to the centre of a sinogram bin, and therefore an interpolation needs to be performed upon histogramming the event into motion-corrected sinograms. In contrast, motion-corrected list-mode event coordinates can be maintained as continuous variables in list-mode reconstruction, thus potentially preserving a higher degree of accuracy in the reconstruction task resulting directly from better sampling of the measurement.

A further potentially significant advantage of list-mode reconstruction may be mentioned. With the continuous improvements in the technology of PET imaging, development of PET scanners capable of encoding time-of-flight (TOF) information, known since the 1980s to potentially reduce the statistical noise variance in PET reconstruction (Snyder and Politte 1983), is being reconsidered. Data generated from such scanners may *only* be reconstructed using the list-mode approach if the TOF information is to be made full use of. This approach, especially in the case of PET scans with high random fractions, is expected to considerably improve image noise behaviour compared to conventional schemes in which TOF information is not incorporated (Kimdon *et al* 2003).

In this work, we are interested in implementing practical list-mode reconstruction algorithms capable of coping with the considerable size of list-mode data (∼250–350 GB/ week) expected to be generated from the HRRT once in fully operational mode. The issue of computation efficiency is therefore a very important one. Accelerated variations of statistical list-mode reconstruction have been investigated, with the aim of reaching and exceeding processing rates of 1.5–2.0 GB h^{-1}, to enable round-the-clock reconstruction of the data expected to be generated by the HRRT. Section 2 introduces the list-mode

expectation maximization reconstruction algorithm. Several accelerated versions of the list-mode algorithm (i.e. subsetized, convergent-subsetized and hybrid) are elaborated in section 3. Contributions of and correction for random (and scatter) events to the reconstruction task will be discussed in section 4, followed by experimental methods and results presented in sections 5 and 6.

2. List-mode expectation maximization reconstruction algorithm

The list-mode expectation maximization (LMEM) reconstruction algorithm can be formulated from first principles (Parra and Barrett 1998), as well as derived from an expression for the likelihood function for statistically independent, Poisson-distributed sinogram data, where the sum over sinogram bins is converted to a summation over events (Huesman *et al* 2000). Denoting λ_j^m as the image intensity in voxel $j (j = 1, \ldots, J)$ at the mth iteration and p_{ij} as the probability of an emission from voxel j being detected along LOR i (often referred to as the 'system matrix'), the resulting LMEM algorithm is given by

$$\lambda_j^{m+1} = \frac{\lambda_j^m}{\sum_{i=1}^{I} p_{ij}} \sum_{k=1}^{N} p_{i_k j} \frac{1}{\sum_{b=1}^{J} p_{i_k b} \lambda_b^m} \tag{1}$$

where i_k refers to the LOR along which the kth list-mode event is detected and N is the number of measured events. The sensitivity correction factor $s_j = \sum_{i=1}^{I} p_{ij}$ is a summation over all possible measurable LORs ($i = 1, \ldots, I$) and calculates the probability of an emission from voxel j being detected anywhere (constructive summation is performed over those LORs for which $p_{ij} \neq 0$).

Initially, EM algorithms were applied to measured data pre-corrected by normalization and attenuation measurements. However, similar to histogram-mode reconstruction schemes, for more appropriate modelling of the measurement process, normalization and attenuation can be incorporated into the LMEM algorithm. Since the probability of attenuation for all points along an LOR is independent of the point of origin along the path for PET, the LMEM algorithm may be properly weighted by simply scaling all elements in a row of the system matrix $P = (p_{ij})_{I \times J}$ by the same factor as calculated by the attenuation and normalization scans. This operation is mathematically equivalent to multiplying P by a diagonal[6] matrix $W = (w_{ii})_{I \times I}$ which allows a weight to be assigned to each LOR, to account for sensitivity variations due to attenuation and normalization.

Such matrix factorization results in the emergence of a cancellation in the algorithm

$$\lambda_j^{m+1} = \frac{\lambda_j^m}{\sum_{i=1}^{I} w_{ii} p_{ij}} \sum_{k=1}^{N} p_{i_k j} \frac{1}{\sum_{b=1}^{J} p_{i_k b} \lambda_b^m}. \tag{2}$$

The cancellation of w_{ii} everywhere, except in the sensitivity factor, which is calculated only once, considerably eases the direct inclusion of normalization and/or attenuation correction. In the case of histogram-mode EM, it has been observed (Michel *et al* 1998) that appropriate modelling of normalization and attenuation as such, results in better image quality when compared to the unweighted case, in which the emission scan is simply pre-corrected by these factors.

[6] This matrix will not be diagonal if one also includes the effects of crystal penetration and inter-crystal scattering. Including such effects results in a high reduction in the sparseness of the matrix and increases the computational demand (Mumcuoglu *et al* 1996).

3. Accelerated reconstruction algorithms

Since the introduction of the ordered subset expectation maximization (OSEM) algorithm for histogram-mode emission tomography by Hudson and Larkin (1994), there has been considerable interest in accelerated image reconstruction techniques. In the OSEM approach, the data are divided into LOR-based subsets, and the image estimate is updated every time the algorithm passes through a data subset.

3.1. Ordinary subsetized list-mode EM algorithm

The histogram-mode data-subset approach can be conceptually applied to list-mode reconstruction as well (Reader *et al* 1998, 2002). One may consider event-based (instead of LOR-based) subsets, obtained by sub-dividing the list-mode data into segments that span a fraction of the total duration of the data[7].

Dividing the data space into L subsets, we use S_l to denote the lth list-mode subset ($l = 1, \ldots, L$). We shall maintain the use of m ($m = 1, 2, \ldots$) as the iteration number which is only completed after a thorough loop through all the L subsets in the data. We also use $\lambda_j^{m,l}$ to denote the image estimate at the mth iteration and lth subset. The subsetized list-mode expectation maximization algorithm (which we shall refer to as the S-LMEM algorithm) is then given by

$$\lambda_j^{m,l} = \frac{\lambda_j^{m,l-1}}{\sum_{i=1}^{I} w_{ii}\, p_{ij}} \sum_{k \in S_l} p_{i_k j} \frac{1}{\sum_{b=1}^{J} p_{i_k b} \lambda_b^{m,l-1}}. \tag{3}$$

One must additionally note here that list-mode subsets exhibit a fundamental difference in comparison to sinogram-based subsets. This is because each list-mode subset can be thought of as a lower-statistics scan in its own right. This observation may point to another advantage of list-mode reconstruction. It has been shown (Takahashi and Ogawa 1997) that the way in which sinogram-data subsets are chosen and ordered has an effect on the resulting reconstructions. The requirement of maximum variation between the data subsets is inherently fulfilled with list-mode subsets.

The aforementioned subsetized algorithm, however, is *not* a convergent algorithm, and instead results in *limit cycles*: oscillatory alternations in image likelihood as well as figures of merit (e.g. contrast, resolution) with further subsets and iterations into the data. Starting from first principles and using the complete data approach as in Hsiao *et al* (2002a, 2002b), Khurd and Gindi (2003) have been able to derive a convergent list-mode EM reconstruction algorithm. The authors have subsequently tested the convergence and speed-up achieved by the algorithm using simulated SPECT data.

In what follows, we show in detail a derivation of the same algorithm using an approach based on re-visiting the histogram-mode technique. We go on to present an intuitive picture of how the algorithm proceeds using additive updates in image space. Furthermore, we propose a hybrid algorithm employing both the regular and convergent list-mode algorithms. Results of implementing the regular, convergent and hybrid algorithms applied to experimental PET data are subsequently presented in section 6. We first discuss issue of convergence as observed and tackled in histogram-mode reconstruction.

[7] For dynamic list-mode image reconstruction, each single frame being reconstructed should in principle be static. With a continually changing object, issues of scanner sensitivity and time resolution limit how short-in-duration a single frame may be in order to obtain sufficient counts. Consequently, in practice, one is likely to encounter a non-static object for a given frame. To deal with this, therefore, it is best (as we have done in our implementation), to have each list-mode subset contain portions of data obtained at *various intervals throughout the frame*, such that all list-mode subsets represent nearly the same object.

3.2. Convergent OSEM reconstruction

In the histogram-mode approach, Hudson and Larkin (1994) were able to prove convergence of the OSEM algorithm *only* for an impractical special case, in which the subsets chosen corresponded to a restrictive 'subset balance' condition in the matrix. In practice, while the algorithm is seen to perform considerably faster than the regular EM algorithm, it is often seen not to converge to a fixed point and instead results in limit cycles. In other words, the OSEM algorithm in itself does not maximize likelihood.

Subsequently, there has been interest in deriving provably convergent versions of the fast OS methods. In Browne and De Pierro (1996), an alternate algorithm termed row-action maximum likelihood algorithm (RAMLA) was proposed along with a convergence proof. The authors have also extended their approach to the case of maximum *a posteriori* (MAP) reconstruction (De Pierro and Yamagishi 2001). Another approach, termed as ordered-subset separable-paraboloidal-surrogate (OS-SPS) algorithm, was also presented in Ahn and Fessler (2003a). One problem with these formulations is that they are controlled by a relaxation schedule to ensure convergence and that there is no easy way to determine these schedules such that they lead to fast algorithms while simultaneously satisfying theoretical criteria to ensure convergence.

Hsiao *et al* (2002a, 2002b) derived a new convergent complete data ordered subsets algorithm for histogram-mode EM reconstruction (C-OSEM). They have shown that the proposed algorithm monotonically decreases the complete data objective function, and furthermore demonstrated that while increase in log likelihood with the iterations is not guaranteed to be monotonic (though the authors have always seen this to be the case); nevertheless, the solution *does* converge to the maximum of the log-likelihood objective function.

We begin by defining C_{ij} as the complete data, as used in statistical derivations of ML-EM, representing the number of counts detected along an LOR i ($i = 1, \ldots, I$) that have originated from voxel j ($j = 1, \ldots, J$). However, one only measures and has knowledge of the incomplete data n_i: total number of counts detected along a given LOR i (regardless of the voxel(s) from which the events have originated), i.e.

$$n_i = \sum_j C_{ij}. \tag{4}$$

Dividing the data space into L LOR-based subsets, S_l is used to denote the lth histogram-mode subset ($l = 1, \ldots, L$). We shall use m ($m = 1, 2, \ldots$) as the iteration number which is only completed after a thorough loop through all the L subsets in the data. We also use $\lambda_j^{m,l}$ to denote the image estimate at the mth iteration and lth subset, while as before p_{ij} is the probability of an emission from voxel j (being detected along LOR i).

In Hsiao *et al* (2002a, 2002b), the provably convergent ordered subset EM (namely C-OSEM) algorithm is given by the following update equations:

$$C_{ij}^{m,l} = n_i \frac{p_{ij}\lambda_j^{m,l-1}}{\sum_{b=1}^{J} w_{ii}\, p_{ib}\lambda_b^{m,l-1}}, \qquad \forall i \in S_l \tag{5}$$

$$\lambda_j^{m,l} = \frac{1}{\sum_{i=1}^{I} w_{ii}\, p_{ij}} \left[\sum_{s=1}^{l} \sum_{i \in S_s} C_{ij}^{m,s} + \sum_{s=l+1}^{L} \sum_{i \in S_s} C_{ij}^{m-1,s} \right] \tag{6}$$

where in the first iteration (i.e. $m = 1$), the above update equation uses the initialization $C_{ij}^{m-1,s} = 0$, while the very first image estimate $\lambda_j^{1,0}$ also needs to be initialized (e.g. all 1s).

In place of the update equation (6), the ordinary OSEM algorithm performs the following:

$$\lambda_j^{m,l} = \frac{1}{\sum_{i \in S_l} w_{ii}\, p_{ij}} \sum_{i \in S_l} C_{ij}^{m,l}. \tag{7}$$

Thus, we see that the C-OSEM algorithm is different from the ordinary OSEM in that the calculation of image updates at every subset (numerator of equation (6)) is *not* limited to the C_{ij} values for LORs in that subset only. Meanwhile, at any subset l, values of C_{ij} ($i \in S_l$) are *updated only* for LORs: this explains why the update image at each subset can be computed nearly as fast as that of regular OSEM.

3.3. Convergent subsetized list-mode EM algorithm

Similar issues, as in the OSEM algorithm, are present in subsetized list-mode reconstruction, and the proposed S-LMEM algorithm results in non-converging (e.g. limit cycles) behaviour, as reported in section 6. Using transformations as in Reader *et al* (1998), one may extend the histogram-mode formulation presented in section 3.2 into list-mode reconstruction. By defining list-mode subsets as event-based subsets, as compared to LOR-based subsets in histogram-mode reconstruction, and replacing the summations over the LORs by summations over the events, while replacing n_i in equation (5) by the numeral 1, it can be shown that one arrives at the following list-mode reconstruction update equations:

$$\tilde{\lambda}_j^{m,l} = \frac{\lambda_j^{m,l-1}}{\sum_{i=1}^{I} w_{ii}\, p_{ij}} \sum_{k \in S_l} p_{i_k j} \frac{1}{\sum_{b=1}^{J} p_{i_k b} \lambda_b^{m,l-1}} \tag{8}$$

$$\lambda_j^{m,l} = \sum_{s=1}^{l} \tilde{\lambda}_j^{m,s} + \sum_{s=l+1}^{L} \tilde{\lambda}_j^{m-1,s} \tag{9}$$

where $\tilde{\lambda}_j^{m,l}$ is an *intermediate* image vector produced by the first update equation (8), subsequently used by equation (9) to arrive at the overall image estimate $\lambda_j^{m,l}$. At the first iteration (i.e. $m = 1$), the initialization $\tilde{\lambda}_j^{m-1,s} = 0$ will be used, while the very first image estimate $\lambda_j^{1,0}$ is initialized to all ones.

One may readily note here that the first step of the convergent approach is similar to the regular subsetized list-mode (S-LMEM) algorithm equation (3). That is, if step 2 of the above approach is replaced by $\lambda_j^{m,l} = \tilde{\lambda}_j^{m,s}$, one arrives at the S-LMEM algorithm. This is *not* the case in the histogram-mode approach, as used by others, since in the OSEM algorithm, at each subset of the data, the sensitivity correction factors depend on the particular subset (given by $\sum_{i \in S_l} w_{ii}\, p_{ij}$), whereas this term does not appear in the update equation (6). On the other hand, since the list-mode data subsets are *event*-based and not LOR-based, the sensitivity correction factors are always given by $\sum_{i=1}^{I} w_{ii}\, p_{ij}$.

As shown in equation (9), the algorithm takes the form of additive updates in image space, in that upon arriving at any subset l, the intermediate image updates which have been previously calculated for other subsets $\{\forall s | s \neq l\}$ are added to the update $\tilde{\lambda}_j^{m,l}$ calculated for the current subset l. We shall refer to this approach as the convergent subsetized list-mode EM (CS-LMEM) algorithm. We also note that it is easy to show that

$$\lambda_j^{m,l} = \lambda_j^{m,l-1} + \tilde{\lambda}_j^{m,l} - \tilde{\lambda}_j^{m-1,l}. \tag{10}$$

From this observation, it follows that by keeping track of the values of $\lambda_j^{m,l-1}$ and the values of $\tilde{\lambda}_j^{m,l}$ for all subsets S_l, $l = 1, \ldots, L$, values of $\lambda_j^{m,l-1}$ can be recursively updated according

to the above relation. This makes the calculation of image updates using the CS-LMEM algorithm nearly as fast as the regular S-LMEM algorithm.

Nevertheless, as we demonstrate in section 6, improvements in image quality achieved by the CS-LMEM algorithm are slower than those obtained using S-LMEM. This has encouraged us to propose and investigate a hybrid algorithm, as we discuss below.

3.4. Hybrid S/CS list-mode EM algorithm

We have found it very useful to investigate the possibility of combining the advantages of the S-LMEM and CS-LMEM algorithms into a hybrid algorithm. Namely, one typically notices, as also shown in section 6, that the regular S-LMEM algorithm, in the first few subsets, is able to produce images of higher quality (e.g. contrast, resolution) relative to the CS-LMEM algorithm, whereas the latter is able to exhibit convergent resolution and contrast behaviour as the iterations proceed. The hybrid approach we have taken uses S-LMEM for the entire or part of the first iteration, followed by CS-LMEM in the rest of the calculation.

4. Random correction in list-mode reconstruction

The contribution of random coincidences to the measurement process has in the past been estimated and taken into account in a number of different approaches depending on the capabilities of the PET scanners being used. Such methods include direct use of the emission data for random correction, an instance of which is the image-based convolution–subtraction technique (Reader *et al* 2001), which estimates the randoms in the object by fitting a function to the random tail outside the object. Work is also currently in progress to incorporate randoms into the system matrix of the EM algorithm by the *estimation* of the *spatial* distribution of randoms contribution (Manavaki *et al* 2002).

For PET systems in which singles rates can be measured during the coincidence measurement process, the singles count rate at the detectors can be used to estimate the randoms distribution (Rokitta *et al* 2000), as we discuss later. Alternatively, a technique to correct for random coincidences is to acquire events arriving within a delayed coincidence window, delayed such that the probability of a true coincidence is zero. In the case of such systems with the delayed-coincidence measurement capability, distribution of random counts can thus be directly measured along with the prompts. In most PET scanners, the prompt data are *precorrected* for the detection of randoms by real-time subtraction of the delayed coincidences, intended to minimize data transfer and processing times.

However, the subtraction can be a source of potential problems: first, the randoms-precorrected data do not follow Poisson statistics. This is because subtraction of delayed coincidences from measured prompts compensates for the coincidence events in terms of the mean but increases the variance. Second, it can result in negative histogram bins, which can be a source of potential problems. The first issue has been tackled by means of practical approximations, such as the shifted Poisson model (Yavuz and Fessler 1996, Qi *et al* 1996), while the second issue has typically been dealt with by zeroing negative sinogram values[8]. The latter can in turn result in positive bias in the final reconstructed image, as reported and discussed later in this paper.

[8] Recently, new likelihood approximations that allow negative sinogram values without requiring zero-thresholding have been proposed (Ahn and Fessler 2003b), which remain to be fully tested.

4.1. Ordinary Poisson EM reconstruction

Separate storage of prompt and delayed events can result in a more accurate reconstruction of the true image activity. The HRRT is an instance of modern PET scanners capable of such measurements. Defining $\bar{r}_i$ and $\bar{s}_i$ as the *expected* randoms and scattered events contributions along any LOR i, one notes that since the prompt events are Poisson by nature, one can consider the log-likelihood function

$$L(\lambda) = \sum_i \left[-\bar{n}_i + n_i^p \ln(\bar{n}_i) \right] \tag{11}$$

where n_i^p is the number of measured prompt events along an LOR i, and $\bar{n}_i$ is the expected number of prompts along the LOR, given by

$$\bar{n}_i = \left\{ \sum_{j=1}^{J} w_{ii}\, p_{ij} \lambda_j \right\} + \bar{r}_i + \bar{s}_i. \tag{12}$$

Application of expectation maximization to the likelihood functions then yields the following 'ordinary Poisson' EM algorithm (Politte and Snyder 1991):

$$\lambda_j^{m+1} = \frac{\lambda_j^m}{\sum_{i=1}^{I} w_{ii}\, p_{ij}} \sum_{i=1}^{I} \frac{w_{ii}\, p_{ij} n_i^p}{\sum_{b=1}^{J} w_{ii}\, p_{ib} \lambda_b^m + \bar{r}_i + \bar{s}_i}. \tag{13}$$

This algorithm poses computational difficulties which need to be addressed. First, we note that a cancellation of w_{ii} in the forward- and back-projection steps is no longer valid, requiring constant look-up of attenuation and normalization factors for LORs along which the events are being read. Furthermore, it must be noted that $\bar{r}_i$ in equation (13) is an *expected* value which *cannot* be appropriately replaced by the *measured* delayed coincidences, rather estimates of mean random counts along the LORs must be used.

To address the latter, two approaches are possible: (i) using singles measurements at the detectors (Rokitta *et al* 2000) to calculate the expected randoms contribution, or (ii) variance reduction (smoothing) for the measured delayed events (Casey and Hoffman 1986, Mumcuoglu *et al* 1996, Badawi *et al* 1999). The first approach has the advantage of utilizing high statistics singles measurements. At the same time, it increases the 'bandwidth' of the scanner, since delayed time windows need not be imposed for delayed coincidence measurements, and less saturation of counts would occur especially for studies involving high count rates.

There are certain difficulties that render the application of either of the aforementioned approaches difficult. Both approaches do require constant look-up of calculated sinograms for the expected random events along the LORs, and as such will introduce additional time-costs to the reconstruction task. As for the first approach, in the HRRT, the singles rates can *only* be measured for the crystal block and *not* the individual crystals. This can result in a relatively coarse estimation of random rates at the individual crystals. This effect is further amplified by noting that while singles are only available for the crystal blocks, each crystal has a different efficiency due to intrinsic as well as object-dependent factors. This is because the contributions of singles events along the various lines passing through a particular crystal depend on the size and shape of the patient. Therefore, one cannot correctly use the trues normalization to compensate for variations in singles rate.

In PET *brain* imaging, compared to other PET modalities, in which a less, though still existent, degree of object variation across the studies is encountered, an approximate technique has been suggested in Rokitta *et al* (2000). It consists of scanning a reference phantom (e.g. a homogeneous cylindrical phantom) and measuring the singles as well as delayed-coincidence

rates, using which the singles rate calibration factors are measured and applied to subsequent patient scans, in which only the singles rates will be measured. This is clearly an approximate technique and remains to be tested and improved further.

Finally, we note that singles measurements need to be corrected for the scatter fraction contained in them. This scatter component also depends on the size and shape of the patient. The above considerations make the application of the single approach difficult, conceptually and computation-wise, and the possibilities and advantages of this technique remain to be fully explored and addressed

The second approach (random smoothing) is currently quite difficult to implement on the HRRT. Due to the non-cylindrical shape of the HRRT as well as the depth-of-interaction measurement capability, the relation between the detector pairs and allocated sinogram bins for the LORs is not 1-to-1, i.e. some projection bins correspond to more than one physical LORs. This problem renders application of variation reduction (smoothing) difficult. In addition, this approach is computationally intensive. The HRRT contains 936 (8×8 dual-crystal) blocks, corresponding to nearly 120k crystals. With no data compression (i.e. mashing), this corresponds to about 3 GB of (floating) random sinograms which need to be processed for each frame if this approach is to be taken. Alternatively, it is possible to take a non-analytic approach to improve variance on randoms measurement; namely, one may acquire them with a noticeably wider time window, but this technique will correspond to a potentially considerable increase in resource allocation and 'bandwidth' consumption, and will result in saturation effects for higher count-rate studies.

4.2. Delayed events subtraction technique

Due to the aforementioned issues as well as the computational difficulties they pose, we have alternatively considered the delayed events subtraction method, as elaborated below, as a practical random correction technique in the implementation of a feasible list-mode reconstruction algorithm applicable to the expected workload of the HRRT. Our approach will involve passing *only* through the list-mode data and does *not* require access to histogrammed data nor processing of them. Furthermore, as shown in section 6, the algorithm does not exhibit the intrinsic bias observed in OSEM when zero-thresholding is applied to negative sinogram bins. Due to its practical implementation, using $\sim$16 processors we have been able to achieve a processing rate of $\sim$1.5 GB h^{-1}, just reaching our feasibility criteria as discussed at the end of section 1.

Scatter correction is yet to be incorporated into the proposed algorithms in this paper. We are currently evaluating different schemes. One possible approach has already been developed for the HRRT, namely the Watson scatter correction technique (Watson 2000). The algorithm is image-based (i.e. computes the scatter contribution using the reconstructed image) and therefore has the practical advantage of being directly applicable to images generated using our proposed methods.

4.3. Sinogram versus image non-negativity constraints

In this work, as explained later, we have imposed an *image non-negativity* constraint in the list-mode reconstruction algorithms. To understand the constraint better, we have performed studies of whether its incorporation into the reconstruction tasks can improve the overestimation bias that is likely to arise from the *sinogram non-negativity* constraint often used in histogram-mode reconstructions, as we describe below.

We first consider the histogram-mode delayed coincidence subtraction technique:

$$\lambda_j^{m+1} = \frac{\lambda_j^m}{\sum_{i=1}^{I} w_{ii}\, p_{ij}} \sum_{i=1}^{I} p_{ij} \frac{n_i^{\text{trues}}}{\sum_{b=1}^{J} p_{ib} \lambda_b^m} \tag{14}$$

with $n_i^{\text{trues}} = n_i^p - n_i^d$ where the measured delayed coincidences are subtracted from the measured prompts. Due to the Poisson nature of prompts and delayed coincidences, it is possible for any bin i to record more randoms than prompts. The constraint $n_i \geqslant 0$ has normally been imposed on the data in previous works (Michel *et al* 1998, 1999), such that the value of n_i is set to zero for any LOR along which a negative value is obtained (i.e. the *sinogram* non-negativity constraint).

Nevertheless, in low-statistics scans, especially those with large random fractions, it is commonly observed that a noticeable number of sinogram bins exhibit negative trues counts after random correction. Imposing the sinogram non-negativity constraint would in turn introduce an *overestimation* bias in the reconstructed images. In this regard, we have instead considered using a weaker condition, namely the *image* non-negativity constraint, such that if upon processing a data subset, the correction to an image voxel is calculated to be negative (due to presence of considerable contribution from negative sinogram bins), the image voxel is not updated for that particular subset[9].

From equation (14), one makes the intuitive observation that by replacing the summation over the LORs with a summation over the number N of measured data (i.e. effectively reading the sinogram counts one by one), and setting n_i to 1, if the histogrammed event was a prompt event, and to -1, if it was a delayed-coincidence event, one arrives at the list-mode reconstruction algorithm:

$$\lambda_j^{m+1} = \frac{\lambda_j^m}{\sum_{i=1}^{I} w_{ii}\, p_{ij}} \sum_{k=1}^{N} p_{i_k j} \frac{\delta_k}{\sum_{b=1}^{J} p_{i_k b} \lambda_b^m} \tag{15}$$

where

$$\delta_k = \begin{cases} 1 & k \text{ is a prompt event} \\ -1 & k \text{ is a delayed coincidence event.} \end{cases} \tag{16}$$

In this study, we implemented the statistical list-mode reconstruction scheme described by equations (15) and (16) for the HRRT. We note that unlike *truly* EM algorithms such as equation (13) for which there is never any 'divide by zero' error, it is possible in the above delayed events subtraction technique that the denominator of equation (15) would be zero (i.e. foreward projection of the current image estimate along the LOR coordinates of a measured event is zero). In such cases, our algorithm neglects the particular events for which this occurs.

The algorithm was accelerated using the three schemes presented in section 3, namely, the S-LMEM, CS-LMEM and hybrid S/CS-LMEM variations. The *image* non-negativity constraint, described earlier, was also imposed. Forward and backward projections were performed using the Siddon projection algorithm (Siddon 1985) for *both* histogram-mode and list-mode reconstructions to allow for direct comparison. We also investigated the parallelization of the list-mode reconstruction code on a Linux cluster.

The algorithms were tested with point source measurements as well as data sets spanning a wide range of count rates in order to investigate resolution, bias, contrast and noise properties for different data acquisition conditions. Convergence properties of the various schemes were also compared in contrast as well as resolution studies.

[9] Due to the multiplicative nature of the iterative EM algorithm, if image voxels were allowed to have negative values, then the subsequent updates would be adversely affected!

5. Methods

5.1. Tomograph

Data were acquired on the second generation of the high resolution research tomographs (HRRT) (Wienhard *et al* 2002). This HRRT scanner has an octagonal design, with the detector heads consisting of a double 10 mm layer of LSO/LYSO for a total of 119 808 detector crystals (crystal size $2.1 \times 2.1 \times 10$ mm^3). The total number of possible LORs is 4.486×10^9.

5.2. Phantoms used and measurements performed

On the HRRT, the data can be axially spanned in various modes. In list-mode reconstruction, however, as discussed in section 1, since the individual LORs are being read one by one, rate of processing the emission data in list-mode is independent of the axial span. One would thus be motivated to explore use of no spanning at all (i.e. span 0). However, performing the normalization measurement in span 0 is extremely time-consuming (as sufficient counts are needed in the LORs), has not yet been implemented on the HRRT and remains to be studied. Therefore, we have instead investigated the effect of switching in-between axial spans of 3 and 9. In histogram-mode reconstruction, processing the data with an axial span of 3 is more expensive than a span of 9 (by nearly three times), whereas this is not the case in list-mode reconstruction.

Two separate experiments were performed as we outline below. In order to allow direct comparison between the various algorithms, consistent axial spans (9 for the first experiment and 3 for the second experiment) were imposed, while a maximum ring difference of 67 was also used. In the second experiment, which involved resolution measurements, the effect of resolution degradation by switching from a span of 3 to a span of 9 was also investigated. In all the reconstructions, 16 subsets were used for the accelerated algorithms. The hybrid S/CS-LMEM algorithm consisted of having the first eight subsets being iterated using the S-LMEM approach and subsequently switching to the CS-LMEM counterpart[10]. The following experiments and analyses were performed:

(a) *Experiment 1*. A 20 cm long, 10 cm radius phantom was used. The phantom had three 5 cm diameter cylindrical inserts: one was solid plastic, one was filled with water (cold insert) and one was filled with a ^{18}F radioactivity concentration of 3.39 μCi ml^{-1} (hot insert). The phantom itself was filled with a ^{18}F concentration of 0.622 μCi ml^{-1} ('background'), yielding a hot insert to background ratio of 5.45. The total amount of radioactivity in the scanner field of view (FOV) at the beginning of the scanning procedure was 4.16 mCi.

A series of 16 20 min long scans was acquired in list-mode, 1 h apart. The measurement thus covered 8.7 radioisotope half-lives, yielding a final amount of radioactivity in the FOV of 0.009 72 mCi. The subset of the scans listed in table 1 was used in the analysis. The listed scans were chosen for analysis so as to cover a random fraction (randoms/trues) range between 8% and 71%, which covers most clinically encountered situations. The following figures of merit were used in evaluating the reconstruction and random correction methods:

(1) *Quantitative accuracy of the random correction*. Reconstructed images were compared with those obtained using the FORE+2D-FBP scheme, since the latter exhibits linearity with measured counts and can be used as a standard for quantitative

[10] This is because we have often observed that the image quality improves rapidly for the first half of the subsets in the *first* iteration of the S-LMEM algorithm, while it begins to exhibit oscillating behaviour for the remaining subsets.

Table 1. Statistics for frames used in the analysis.

Index	Total activity (mCi)	Trues rate (kcps)	Random fraction (%)
1	2.7	814	70.9
2	1.8	591	46.8
3	1.3	425	32.0
4	0.95	208	16.2
5	0.19	69	7.73

accuracy. ROIs were selected on the hot and cold as well as the background regions of the reconstructed images for each of the studies frames. Five transaxial planes were selected for the calculation of mean and standard deviation of total counts in the ROIs. Tests of quantitative accuracy were performed for the 3D-OSEM algorithm (with (a) no random correction, (b) the sinogram non-negativity constraint and (c) the image non-negativity constraint) as well as the S-LMEM algorithm.

(2) *Image random fractions*. For each list-mode reconstructed frame from table 1), an *image random fraction* (RF = randoms/trues) was measured using

$$\text{image RF} \equiv \left[\sum_{j=1}^{J} \lambda_j^{\text{nrc}} \Big/ \sum_{j=1}^{J} \lambda_j^{\text{rc}} \right] - 1 \tag{17}$$

where λ_j^{rc} and λ_j^{nrc} are reconstructed image intensities at a voxel j with/without random correction being performed, respectively. As such, the image random fractions were calculated and compared for images reconstructed using the S-LMEM algorithm. Image RF values are not expected to be numerically equivalent to the random fraction in the acquired data: the true and the random events have a different spatial distribution and will therefore be differently affected by attenuation and sensitivity corrections. However, the ratio between the image RF and the acquired events RF must not vary as a function of acquisition condition if no count rate or number of counts dependent bias is introduced in the data by the random corrections.

(3) *Contrast versus noise comparisons*. Contrast versus noise studies were performed for images reconstructed up to three iterations using the 3D-OSEM, S-LMEM, CS-LMEM and hybrid S/CS-LMEM algorithms. The contrast and the noise were estimated following approximately the NEMA NU 2001 protocol. For any given axial plane, the per cent contrast Q_H for the hot cylinder was calculated by

$$Q_H = \frac{C_H/C_B - 1}{A_H/A_B - 1} \times 100\% \tag{18}$$

where C_H and C_B are the average counts in regions of interest (ROIs) placed on the reconstructed images of the hot insert and the background region, respectively, and A_H/A_B is the actual concentration ratio between the two regions (measured to be 5.45). The percentage noise (standard deviation/mean) was calculated by placing eight ROIs on different parts of the background image and averaging their values to yield a background mean value and its standard deviation.

(b) *Experiment 2*. Using a technique (Sossi *et al* 2003) that allows printing of radioactive point sources using a modified standard ink-jet printer, we imaged radioactive (^{18}F) point sources of size 0.7 mm placed at $X = 0, 1, 2, 3, 4, 5$ and 6 cm radially away from the centre of the FOV. In order to study improvements in resolution with further iterations of the data, plots of the measured FWHM versus iteration (for two selected point sources 1 and 5 cm away from the centre of the FOV) were calculated and shown for three iterations of

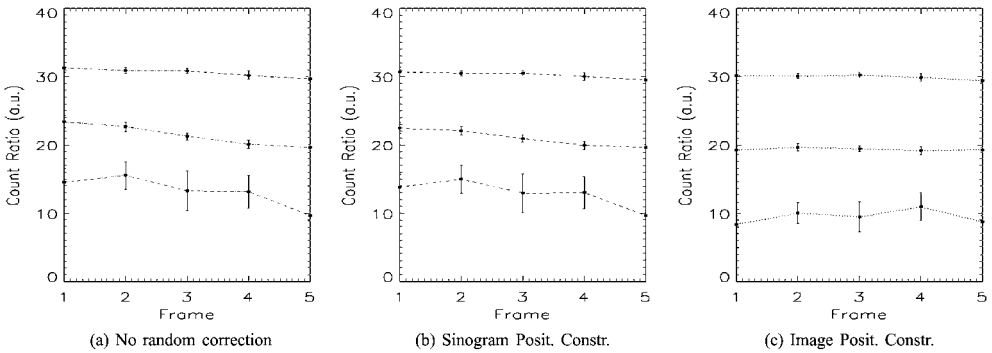

Figure 1. Calculated *ratios* between total counts for images reconstructed using 3D-OSEM and those obtained using FORE-2D-FBP, for the hot (top), background (middle) and cold (bottom) regions of the phantom. For better visibility, the plots have been shifted by ten units with respect to one another. The case of reading 10m counts is shown, and qualitatively similar results have been observed in the 40m and 80m cases. The error bars indicate statistical variation for the five transaxial planes selected.

the 3D-OSEM, S-LMEM, CS-LMEM and hybrid S/CS-LMEM reconstruction schemes. Plots of the measured FWHM versus radial position were also depicted for these four schemes to compare the final reconstructed FWHM values across the FOV. The overall FWHM for any given point was measured by calculation of the root mean squared value of the measured point widths in the the transaxial (X, Y) and axial (Z) directions.

We have also studied effects of degradation in resolution as one switches from (axial) span 3 reconstruction to span 9. The latter is expected to result in poorer FWHM values along the *axial* (Z) direction and is expected to degrade further with increasing distances from the centre of the FOV. Values of overall FWHM versus iteration were plotted for two point sources at $X = 3$ cm and 5 cm from the centre of the FOV. The measured degradation in FWHM (along the Z direction) versus radial position were also depicted for the S-LMEM, CS-LMEM and hybrid S/CS-LMEM reconstruction schemes.

5.3. Code parallelization

The code parallelization was implemented on the University of British Columbia Department of Meteorology Linux Monster Cluster[11]: a 128 × IBM eServers × 330 with dual Pentium III: 1 GHz, 1 GB RAM, 256 KB cache system. The message passing interface (MPI) software was utilized to parallelize the list-mode reconstruction code. The algorithm essentially consists of having several slave nodes to perform the actual forward and backward projections, results of which are passed to the master node for updating the current image estimate after every subset.

6. Results

6.1. Experiment 1: contrast phantom

Figure 1 shows plots of *ratios* between ROI counts in images reconstructed using 3D-OSEM and those obtained using FORE+2D-FBP. In each figure, three plots are shown corresponding to ROIs in the hot, background and cold regions. Figures 1(a)–(c) correspond to cases where 3D-OSEM was performed: (a) without any random correction, (b) with the sinogram non-negativity constraint and (c) with the image non-negativity constraint. The data reconstructed

[11] http://www.gdcfd.ubc.ca/Monster/.

Table 2. Image bias for 3D-OSEM reconstruction of frames 1 and 5 in table 1 (10m counts).

	No random correction	Sinogram positron construction
Frame 1		
Hot	3.8%	1.8%
Background	21.7%	17.1%
Cold	74.0%	65.2%
Frame 5		
Hot	0.9%	0.4%
Background	1.8%	1.9%
Cold	10.4%	10.0%

contained 10m counts. The reason this comparison was performed for the 3D-OSEM algorithm was because a similar comparison is not possible in list-mode reconstruction, for which the sinogram non-negativity constraint cannot be imposed.

In figure 1(c), the values are seen to be consistent (within statistical error) for a wide range of event random fractions (8–71%). This is seen *not* to be the case in the former two schemes, especially for the background and cold regions, which contain less trues and therefore are more sensitive to insufficient random correction. One is therefore clearly able to verify that, as predicted, imposing the sinogram non-negativity constraint can introduce an *overestimation* bias in the reconstructed images, especially for low-statistic scans.

Table 2 shows percentage increase in ROI counts density for 3D-OSEM reconstructed images of frames 1 and 5 (71% and 8% random fractions) when reconstructed using schemes (a) and (b), when measured in comparison to the case of reconstructing with the *image* non-negativity constraint only. Schemes (a) and (b) are seen to exhibit close values for overestimation bias percentages in each of the hot, background and cold regions, which can be explained by the low-statistic nature of the scans (10m counts) resulting in a notable fraction of histogram bins to measure more randoms than prompts, which are subsequently neglected in scheme (b). Similar qualitative patterns have also been observed in the cases of having 40m and 80m counts, with the difference that bias is seen to become less significant in scheme (b) (e.g. 54% for 40m counts and 35% for 80m counts, in cold region).

Testing quantitative accuracy for the list-mode algorithm, figure 2 shows similar plots of *ratios between* images reconstructed using S-LMEM and FORE+2D-FBP. The plots are also seen to be consistent (within statistical error) for the hot, cold and background regions. Consequently, the S-LMEM algorithm is seen to preserve reconstructed counts in various parts in the image for a wide range of random fractions.

Ratios of random fractions. Image random fractions, calculated as described in the previous section, along with random fraction of the acquired events are shown in table 3. The two values are not expected to be equal, as explained in the methods section, but for an accurate list-mode random correction technique, they are expected to have same ratios independent of particular frame. As can be seen from the table, there is only a very small change in the ratios over a wide range of random fractions.

Contrast versus noise comparison. Monitoring progression of image quality with iteration, figure 3 shows contrast versus noise plots for three iterations (16 subsets with results after every four subsets shown) of S-LMEM as well as 3D-OSEM on frame 4 (with random fraction of 16%). We have verified, for the wide range of random fractions and total counts considered, that the S-LMEM algorithm performs at least as effectively (in terms of contrast versus noise) as 3D-OSEM. We have also seen, as shown in figure 3, that both algorithms

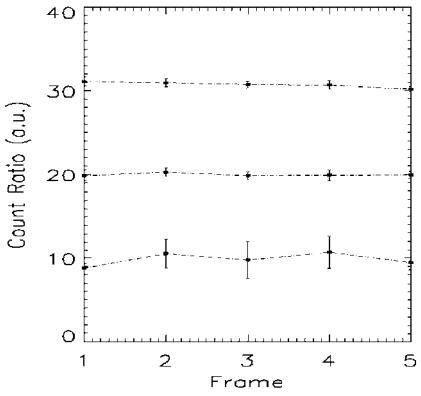

Figure 2. Calculated ratios between total counts for images reconstructed using S-LMEM and those obtained using FORE-2D-FBP, for the hot (top), background (middle) and cold (bottom) regions of the phantom. For better visibility, the plots have been shifted by ten units with respect to one another. The case of 10m counts is shown, and qualitatively similar results have been observed in the 40m and 80m cases. The error bars indicate statistical variation for the five transaxial planes selected.

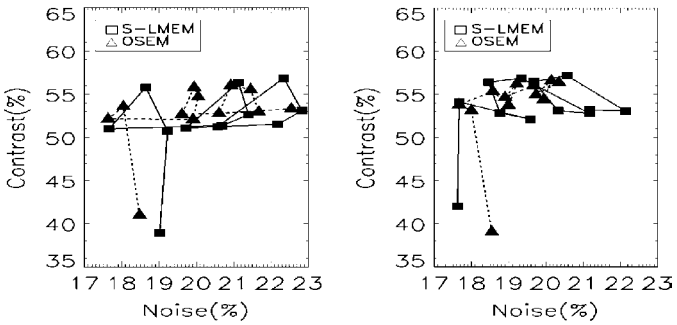

Figure 3. Contrast versus noise plot for images reconstructed with S-LMEM and OSEM. Three iterations are performed with 16 subsets, with results shown every 4 subsets. Results are shown for (a) 20m and (b) 40m total counts. Presence of limit cycles is noticeable in both algorithms.

Table 3. Table of random fractions.

Index	Events RF	Image RF	Image RF/events RF (%)
1	70.9	45.8	65.7
2	46.8	31.0	66.7
3	32.0	21.2	66.8
4	16.2	10.7	65.7
5	7.73	5.19	67.2

exhibit limit cycles, commonly reported in the literature to arise from subsetization of the measured data.

Figures 4(a), (b) show plots of contrast versus noise for images reconstructed using three iterations of the S-LMEM, CS-LMEM and hybrid S/CS-LMEM algorithms. One is able to

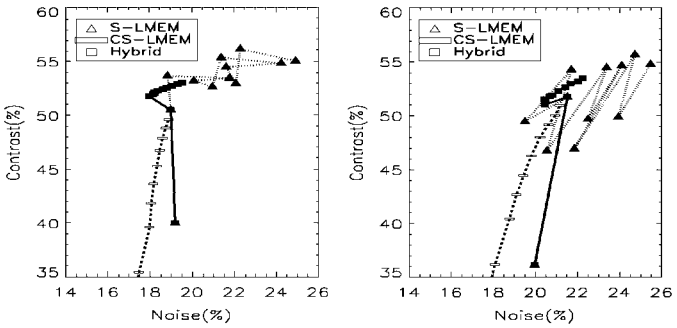

Figure 4. Contrast versus noise plots for images reconstructed using the S-LMEM (dotted), CS-LMEM (- -) and hybrid S/CS-LMEM (solid) algorithms with scan durations containing (a) 10m and (b) 5m total counts. Three iterations are shown.

clearly observe limit cycles in the ordinary S-LMEM approach, especially with lower statistics. The CS-LMEM approach, on the other hand, is able to eliminate the observed limit cycles. Using the hybrid technique, in order to combining the advantages of the S-LMEM and CS-LMEM algorithms (as explained in section 3.4), the plots show that one is able to attain higher contrast values in a lower number of iterations, and yet maintain the non-cyclical behaviour as the reconstruction proceeds.

6.2. Experiment 2: printed point sources

Figures 5(a), (b) show plots of reconstructed FWHM width versus iteration for point sources located at $X = 1$ cm and 5 cm from the centre of FOV, with the data reconstructed using the 3D-OSEM, S-LMEM, CS-LMEM and hybrid S/CS-LMEM algorithms. The values of FWHM resolution are seen to change in a cyclical manner for the 3D-OSEM and S-LMEM algorithms. In figure 5(a), for instance, the FWHM width reconstructed using the S-LMEM approach is seen to oscillate between a low of 3.17 mm and a high of 3.23 mm. Nevertheless, one clearly observes that in the CS-LMEM approach, due to its converging behaviour, the FWHM widths improve with further iterations in a systematic and predictable manner. One is also able to observe that the hybrid approach results in a faster decrease in reconstructed FWHM width with less iterations while maintaining the non-cyclical behaviour.

Figure 5(c) shows plots of measured FWHM values after four iterations for all the seven points located at $X = 0, 1, 2, 3, 4, 5, 6$ cm from the centre of FOV. We note from the plots that the histogram-mode and list-mode algorithms are able to achieve nearly similar FWHM values for a given point. One is also able to observe *space-variance* of the point spread function, manifesting itself as a degradation in resolution as one moves away from the centre of the FOV (seen in all the reconstruction tasks). This effect occurs due to a higher probability of inter-crystal penetration with higher angles of radiation incident on crystal fronts. Depth-of-interaction (DOI) encoding is known to improve this problem, but has not reached complete space-invariance. An attempt has been made in Rahmim *et al* (2003) to model the space-variance and anisotropicity of the point-spread function into the system matrix of the EM algorithm for the HRRT.

Plots of FWHM versus iteration for point sources at $X = 3$ cm and 5 cm from the centre of the FOV are shown in figure 6(a). The image has been reconstructed using the hybrid algorithm with axial spans of 3 and 9. It is seen, as expected, that the effect of axial spanning is more significant for the point source more distant from the centre of the FOV. To see this

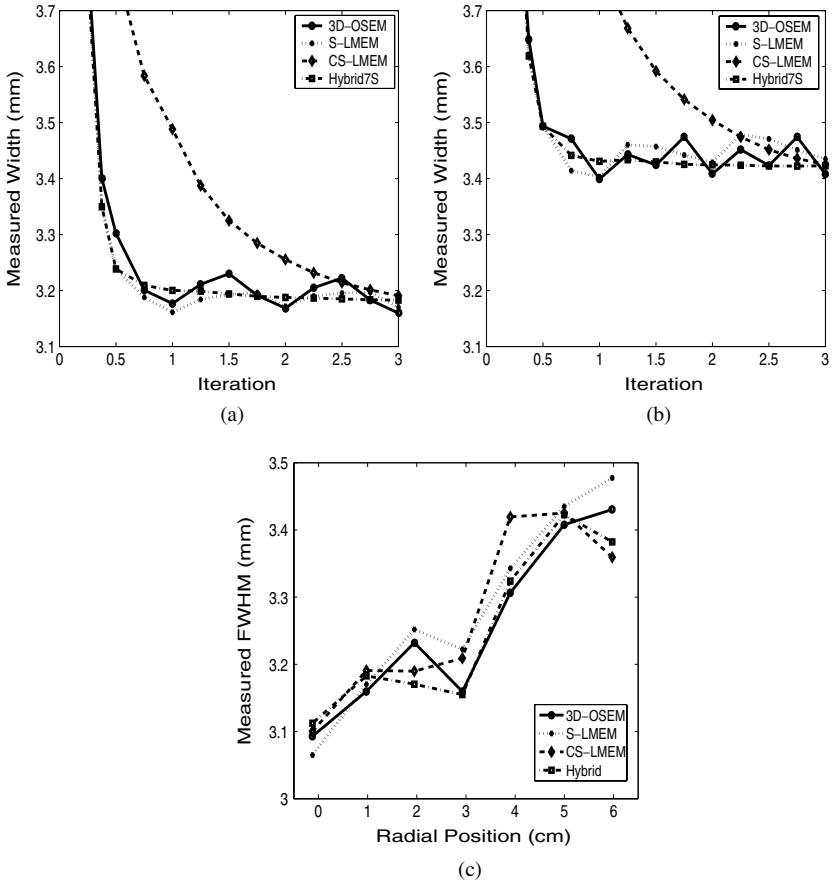

Figure 5. Plots of reconstructed FWHM width versus iteration are shown for the 3D-OSEM, S-LMEM, and the CS-LMEM and hybrid algorithms for the point source located at (a) 1 cm and (b) 5 cm from centre of the FOV. (c) Final FWHM values are shown for all the reconstructed points sources using the aforementioned four schemes (after three iterations).

more clearly, figure 6(b) shows plots of final FWHM values (along the Z-direction) for the various point sources reconstructed using the S-LMEM, CS-LMEM and hybrid algorithms. The resolution along the Z-direction is seen to degrade further as one moves away from the centre of the FOV for the various schemes. We have also checked the resolution along the transaxial direction and have observed no change to occur upon switching in-between the axial spans, as expected, since this is only expected to affect the resolution in the Z-direction.

Parallelization of the reconstruction task. Parallelization was successfully implemented using MPI for the list-mode algorithms. It was found that having the slave nodes indirectly accessing list-mode data *did* improve the efficiency compared to the case of the master node distributing the actual workload to all the processor. This required multiple read access to a single file as supported by the cluster. An instance of parallelization performance using the scheme described is shown in figure 7, where a frame with 40m total counts was reconstructed. By direct fitting (as explained in the figure), it was found that by dividing the 40m frame into 1, 8, 16, 32 and 64 subsets, 99%, 98%, 97%, 94% and 88% of the workload were parallelized, respectively. With this data on the cluster, using 16 subsets and 16 processor, we are able to

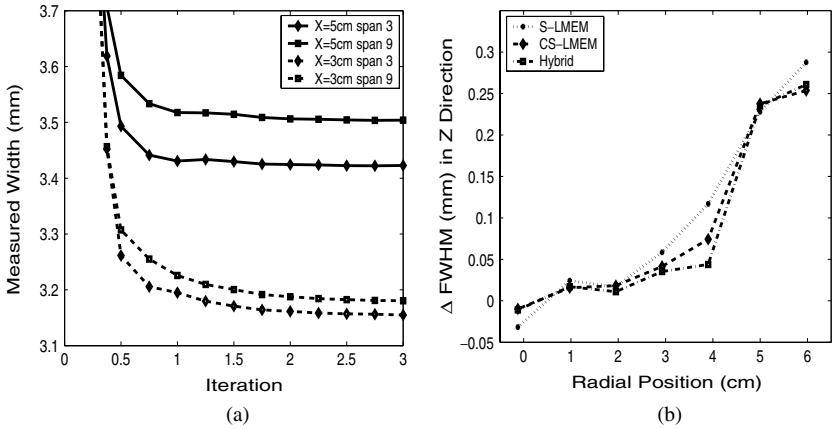

Figure 6. (a) Overall FWHM versus iteration for images reconstructed using the hybrid S/CS-LMEM algorithm: point sources located at 3 cm and 5 cm from centre of FOV are shown. (b) Degradation in FWHM (along the Z-direction) versus radial position are shown for all the reconstructed points sources using the S-LMEM, CS-LMEM and hybrid schemes (after three iterations).

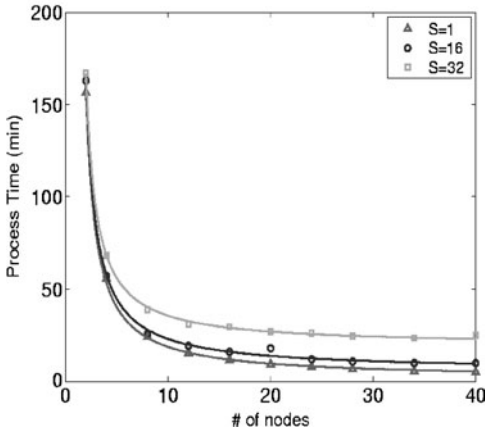

Figure 7. Process Time (T) versus number of nodes (N) for a frame with 40m counts is shown. It is readily observed that decreasing the number of subsets increases the efficiency. The points are fit with $T = T_0(\frac{p}{N-1} + (1-p))$, where $N-1$ is the number of slave nodes in MPI and p represents the percentage of reconstruction parallelized.

reach a processing rate of 1.5 GB h^{-1}. This figure is very preliminary and is expected to only improve in the near future with increased processing power as well as reconstruction software optimization.

7. Conclusion

Practical statistical list-mode reconstruction algorithms were developed for the high-resolution research tomograph (HRRT). Various random correction schemes applicable to the HRRT were discussed, and the list-mode delayed events subtraction method was implemented as a practical random correction technique. An *image* non-negativity constraint was employed in

the algorithm. This constraint was shown, using comparisons in histogram-mode 3D-OSEM reconstruction, to effectively remove the overestimation bias typically encountered when a *sinogram* non-negativity constraint is used. Quantitative accuracy of the random-corrected images for a wide range of random fractions was demonstrated in different regions of list-mode reconstructed images. Results also indicated that images were comparable in terms of statistical properties, contrast versus noise as well as resolution with images generated by 3D-OSEM.

Using regular subsetized list-mode reconstruction, we were able to observe limit cycles: oscillatory alternations in image quality parameters (such as contrast and resolution) with further subsets and iterations into the data, similar to what is commonly encountered in ordered subset histogram-mode reconstruction. To address this issue, we implemented a convergent list-mode EM reconstruction algorithm, based on an extension of previous work by Hsiao *et al* (2002a, 2002b) in histogram-mode reconstruction, and investigated its properties using experimental PET data. It was demonstrated that the algorithm is robust and does not result in limit cycles.

A hybrid algorithm combining the advantages of the ordinary and the convergent list-mode algorithms was also proposed, and was shown to combine the advantages of the two methods (i.e. it was able to reach a higher image quality in a lower number of iterations while maintaining a convergent behaviour), making it a good alternative to the ordinary subsetized list-mode EM algorithm.

Acknowledgments

This work was supported by the Canadian Institute of Health Research, the TRIUMF Life Science grant, the Natural Sciences and Engineering Research Council of Canada UFA (VS) and PGS B (AR) scholarships, as well the Michael Smith Foundation for Health Research scholarship (VS). Part of the computation was performed on the University of British Columbia Department of Meteorology Linux Monster Cluster, for which the authors wish to express gratitude. The authors are also indebted to Paul Piccioni for providing his expertise in the radioactive printing experiments.

References

Ahn S and Fessler J 2003a Globally convergent ordered ubsets algorithms for emission tomography using relaxed oredred subsets algorithms *IEEE Trans. Med. Imaging* **22** 613–26

Ahn S and Fessler J A 2003b Statistical emission image reconstruction for randoms-precorrected PET scans using negative sinogram values *IEEE NSS & MIC 2003 Conf. Rec. (Portland, OR, Oct. 2003)*

Badawi R D, Miller M P, Bailey D L and Marsden P K 1999 Randoms variance-reduction in 3D-PET *Phys. Med. Biol.* **44** 941–54

Browne J and De Pierro A 1996 A row-action alternative to the EM algorithm for maximizing likelihoods in emission tomography *IEEE Trans. Med. Imaging* **15** 687–99

Casey M E and Hoffman E J 1986 Quantitation in positron emission tomography: 7. A technique to reduce noise in accidental concidence meansurements and coincidence efficinecy calibration *J. Comput. Assist. Tomogr.* **10** 845–50

De Pierro A R and Yamagishi M E B 2001 Fast EM-like methods for maximum *a poteriori* estimates in emission tomography *IEEE Trans. Med. Imaging* **20** 280–8

Hsiao I T, Rangarajan A and Gindi G 2002a A provably convergent OS-EM like reconstruction algorithm for emission tomography *Conf. Rec. SPIE Med. Imaging* **4684** 10–19

Hsiao I T, Rangarajan A and Gindi G 2002b A new convergent MAP reconstruction algorithm for emission tomography using ordered subsets and separable surrogates *Conf. Rec. IEEE Int. Symp. Biomed. Imaging* 409–12

Hudson H M and Larkin R S 1994 Accelerated image reconstruction using ordered subsets of projection data *IEEE Trans. Med. Imaging* **13** 601–9

Huesman R H, Klein G J, Moses W W, Qi J, Reutter B W and Virador P R G 2000 List mode maximum likelihood reconstruction applied to positron emission mammography with irregular sampling *IEEE Trans. Med. Imaging* **19** 532–7

Khurd P K and Gindi G R 2003 A globally convergent ordered-subset algorithm for list-mode reconstruction *IEEE NSS & MIC 2003 Conf. Rec. (Portland, OR, Oct. 2003)*

Kimdon J A, Qi J and Moses W W 2003 Effect of random and scatter fractions in variance reduction using time-of-flight information *IEEE NSS & MIC 2003 Conf. Rec. (Portland, OR, Oct. 2003)*

Manavaki R, Reader A J, Keller C, Missimer J and Walledge R J 2002 Scatter modelling for 3-D PET list-mode EM reconstruction *IEEE NSS & MIC 2002 Conf. Rec. (Norfolk, VA, Nov. 2002)*

Michel C, Liu X, Sanabria S, Lonneux M, Sibomana M, Bol A, Comtat C, Kinahan P E, Townsend D W and Defrise M 1999 Weighted schemes applied to 3D-OSEM reconstruction in PET *IEEE Nucl. Sci. Symp. Conf. Record* **3** 1152–7

Michel C, Sibomana M, Boi A, Bernard X, Lonneux M, Defrise M, Comtat C, Kinahan P E and Townsend D W 1998 Preserving Poisson characteristics of PET data with weighted OSEM reconstruction *IEEE Nucl. Sci. Symp. Conf. Record* **2** 1323–9

Mumcuoglu E U, Leahy R M and Cherry S R 1996 Baysian reconstruction of PET images: methodology and performance analysis *Phys. Med. Biol.* **41** 1777–807

Mumcuoglu E U, Leahy R M, Cherry S R and Hoffman E 1996 Accurate geometric and physical response modelling for statistical image reconstruction in high resolution PET *IEEE Nucl. Sci. Symp. Conf. Record.* **3** 1569–73

Parra L and Barrett H H 1998 List-mode likelihood: EM algorithm and image quality estimation demostrated on 2-D PET *IEEE Trans. Med. Imaging* **17** 228–35

Politte D G and Snyder D L 1991 Corrections for accidental coincidences and attenuation in maximum-likelihood image reconstruction for positron-emission tomography *IEEE Trans. Med. Imaging* **10** 82–9

Qi J, Leahy R M, Hsu C, Farquhar T H and Cherry S R 1996 Fully 3D Baysian reconstruction for the ECAT EXACT HR+ *IEEE Trans. Nucl. Sci.* **45** 1096–103

Rahmim A, Bloomfield P, Houle S, Lenox M, Michel C and Sossi V 2003 Motion Correction in Histogram-Mode and List-Mode EM Reconstructions *IEEE NSS & MIC 2003 Conf. (Portland, OR, Oct. 2003)*

Rahmim A, Lenox M, Michel C, Reader A J and Sossi V 2003 Space-variant and anisotropic resolution modelling for list-mode EM reconstruction *IEEE NSS & MIC 2003 Conf. Rec. (Portland, OR, Oct. 2003)*

Reader A J, Ally S, Bakatselos F, Manavaki Roido, Walledge R, Jeavons A P, Julyan P J, Zhao S, Hastings D L and Zweit Jamal 2002 One-pass list-mode EM algorithm for high-resolution 3-D PET image reconstruction into large arrays *IEEE Trans. Nucl. Sci.* **49** 693–9

Reader A J, Erlandsson K, Flower M A and Ott R J 1998 Fast accurate iterative reconstruction for low-statistics positron volume imaging *Phys. Med. Biol.* **43** 835–46

Reader A J, Zhao Sha, Julyan P J, Hastings D L and Zweit J 2001 Adaptive correction of scatter and random events for 3-D backprojected PET data *IEEE Nucl. Sci. Trans.* **48** 1350–6

Rokitta O, Casey M, Wienhard K and Pictrzyk U 2000 Random correction for positron emission tomography using singles count rates *IEEE Nucl. Sci. Symp. Conf. Record.* **3** 37–40

Siddon R L 1985 Fast calculation of the exact radiological path for a three-dimensional CT array *Med. Phys.* **12** 252–5

Snyder D L and Politte D G 1983 Image reconstruction with list-mode data in an emission tomography system time-of-flight measurements *IEEE Trans. Nucl. Sci.* **20** 1843–9

Sossi V, Buckley K R, Piccioni P, Rahmim A, Camborde M-L and Ruth T J 2003 Printed sources for positron emission tomography (PET) *IEEE NSS & MIC 2003 Conf. Rec. (Portland, OR, Oct. 2003)*

Takahashi M and Ogawa K 1997 Selection of projection set and the order of calculation in ordered subsets expectation maximization method *IEEE Nucl. Sci. Symp.* **2** 1408–1412

Watson C C 2000 New, Faster, Image-Based Scatter Correction for 3D PET *IEEE Trans. Nucl. Sci.* **47** 1587–94

Wienhard K *et al* 2002 The ECAT HRRT: performance and first clinical application of the new high resolution research tomograph *IEEE Trans. Nucl. Sci.* **49** 104–10

Yavuz M and Fessler J A 1996 Objective functions for tomographic reconstruction from randoms-precorrected PET scans *Proc. IEEE Nuclear Science Symp. Medical Imaging Conf. (Anaheim, CA)* **2** 1067–71